nature communications

Article

https://doi.org/10.1038/s41467-025-67458-1

Single iron redox sites boost Methanol-SCR at low temperature

Received: 26 November 2024

Accepted: 1 December 2025

Published online: 20 December 2025

Check for updates

Han Sun[1,2,8], Dekai Liu[1,8], Chenyang Li[1], Chang Wang[3], Haijun Chen[1,4] ✉, Zhili Wang[5], Guangjin Hou[5] ✉, Yun Hu[4], Masaaki Kitano[6], Xiaobo Li[7], Ke Li[7], Haoran Yang[7], Mian Wei[7], Zhaoyu Xiao[7] & Weili Dai[3] ✉

Selective catalytic reduction of NO_x to N_2 by methanol as a reducing agent presents a prospective solution for the removal of NO_x from the exhaust of methanol engines and the coal-fired power plant, but it confronts the problem of insufficient deNO_x activity at low temperatures (<350 °C). Here, we discover a strategy for boosting the activity of low-temperature Methanol-SCR by the collaboration of zeolitic acid sites with single iron redox sites. The further pilot-scale bench test using the coated monolithic catalyst also exhibits a remarkable NO_x conversion and a high stability at low temperature. The location of different Fe sites in FER zeolite is identified by X-ray absorption spectroscopy, Mössbauer spectroscopy, as well as 2D ^{1}H-^{1}H DQ MAS NMR technology. While the dynamic evolution of $[FeO]^+$ as the critical redox site for NO oxidation is successfully captured by in situ Mössbauer spectroscopy, which unravels the mechanism for the generation of key intermediate HONO on $[FeO]^+$ sites contributing the low-temperature Methanol-SCR activity. These results indicate the great potential application of Fe-FER zeolite catalyst in industrial Methanol-SCR and provide an atomic-level comprehension of how the dual-active-sites contribute to low-temperature Methanol-SCR activity.

The application of methanol as a leading alternative-fuel candidate is growing steadily in the transportation field owing to its economy and easy-to-store[1]. Approximately 90% less CO_2 emissions running on methanol engines using green methanol than conventional liquid fuels are very attractive under the objective of carbon neutrality[2]. Despite the utilization of methanol fuel drastically reduces sulfur and particulate emissions, the emission of NO_x is still existing issue. Selective catalytic reduction technology by NH_3 (NH_3-SCR) is currently one of the most widely used technologies for NO_x abatement[3–5]. However, in the exhaust gas emitted from methanol as fuel, toxic HCN will be generated in NH_3-SCR process inevitably as a consequence of the reaction of NH_3 with HCHO[6]. Moreover, NH_3-SCR process also confronts a difficulty for the deNO_x treatment in some application scenarios containing high concentrations of SO_x, such as coal-fired power plants and marine diesel engines using heavy fuel oil (HFO). Ammonium sulfates are known to be a deactivation species for SCR catalysts according to the inevitable side reaction between NH_3 and SO_x, which usually leads to the deactivation of catalysts and pipe blockage[7]. Methanol as a reducing agent instead of NH_3 can avoid the formation of ammonium sulfates and the utilization of methanol from exhaust directly as a reducing agent for NO_x removal, not only enhancing the safety of the deNO_x process, but also saving space for the storage of

[1]Department of Electric Science and Engineering, College of Electronic Information and Optical Engineering, Nankai University, Tianjin, China. [2]School of Chemical Engineering, Zhengzhou University, Zhengzhou, China. [3]School of Materials Science and Engineering, Nankai University, Tianjin, China. [4]National Engineering Laboratory of VOCs Pollution Control Technology and Equipment, School of Environment and Energy, South China University of Technology, Guangzhou, China. [5]State Key Laboratory of Catalysis, iChEM, Dalian Institute of Chemical Physics, Chinese Academy of Sciences, Dalian, China. [6]MDX Research Center for Element Strategy, International Research Frontiers Initiative, Tokyo Institute of Technology, Midori-ku, Yokohama, Japan. [7]Shanghai Marine Diesel Engine Research Institute, Shanghai, China. [8]These authors contributed equally: Han Sun, Dekai Liu. ✉e-mail: chenhj@nankai.edu.cn; ghou@dicp.ac.cn; weilidai@nankai.edu.cn

deNO$_x$ reductant. Accordingly, selective catalytic reduction NO$_x$ to N$_2$ by methanol (Methanol-SCR) is a prospective technology for the deNO$_x$ treatment both in the combustion of conventional fuels and promising methanol fuel.

Methanol-SCR catalysts have been developed by supported metal or metal oxide, such as Al_2O_3-based catalysts and zeolite-based catalysts[8–11]. However, the deNO$_x$ efficiency for Methanol-SCR on the above-reported catalysts is nowhere close to that of NH$_3$-SCR on the commercialized V-based oxide deNO$_x$ catalysts, especially at low temperature (<350 °C). The rational design of catalysts with high activity requires guidance based on an understanding of the structural features, which is vital for establishing the relationship between the structure of the catalyst and its performance during the reaction. Generally, the strong acidity and excellent redox property are two crucial factors for designing NH$_3$-SCR catalysts[12,13]. Strong and abundant acidity is conducive to the adsorption of NH_3/NH_4^+ species, which react either with adsorbed nitrites/nitrates following the Langmuir −Hinshelwood (L-H) mechanism or directly with gaseous NO$_x$ following the Eley−Rideal (E-R) mechanism. Prominent redox ability is favorable to the formation of active NH$_2$ or gaseous NO$_2$ intermediates, which can improve the deNO$_x$ efficiency through the E-R mechanism or "Fast SCR", respectively. Likewise, the acidity and redox properties are pivotal for the Methanol-SCR catalyst to adsorb/activate methanol and NO$_x$, respectively. The framework aluminum sites in zeolites, namely Brønsted acid sites (BASs), can effectively control the adsorption and activation of methanol molecules[14–16]. The presence of extra-framework aluminum (EFAL) species as Lewis acid sites (LASs) in the pores of zeolite has also been reported to accelerate the activation of methanol by exerting a big influence on the acid strength of BAS[17,18]. Abundant and strong acidity contributes to the adsorption/activation of methanol molecules is essential for Methanol-SCR catalysts, has been reported according to our previous research[19]. However, the direct synthesis of H-FER zeolite with the controllable amounts of extra-framework aluminum (EFAL) species is very difficult and with poor repeatability, thus it is not conducive to industrial applications. Additionally, Bi-FER zeolite with the controllable Bi amounts was prepared for improving the low-temperature Methanol-SCR activity, while the yield of N$_2$O as the by-product was also highly enhanced[20]. Therefore, a potential industrial Methanol-SCR catalyst with remarkably low-temperature activity and low cost is still highly required. HONO has also been proposed as an intermediate participant in the Methanol-SCR reaction by adsorbing on EFAL species to form nitrites, which can further react with methyl groups produced on BASs to generate the key intermediate CH_3NO_2[19]. The formation of HONO is closely related to NO, NO$_2$, and H$_2$O. Redox sites are favorable to the formation of active intermediates during the NH$_3$-SCR reaction. Therefore, excellent redox properties to promote the NO oxidation and the generation of HONO by the reaction of NO$_x$ with H$_2$O are equally important in Methanol-SCR catalysts.

Herein, we developed a series of Fe-FER zeolites as Methanol-SCR catalysts, of which the structural features contain the acidity of the zeolite and the redox property of Fe sites. The introduction of Fe enhances the catalytic activity of Methanol-SCR on FER zeolite remarkably at the low temperature region (250-350 °C). Atomic-level exploration of Fe sites under SCR remains obscure due to the complexity of Fe active sites and a lack of direct observation of the catalytic performance on specific sites. But in this work, the geometric configurations and atomic compositions, as well as the location of different Fe sites in FER zeolite, were distinguished precisely by multi-characterization methods such as spherical aberration-corrected high-angle-annular-dark-field scanning transmission electron microscopy (HAADF-STEM), X-ray absorption spectroscopy (XAS), Mössbauer spectroscopy, as well as 2D ^{1}H-^{1}H double quantum Magic Angle Spinning Nuclear Magnetic Resonance (2D ^{1}H-^{1}H DQ MAS NMR) technology. The dynamic evolution of $[FeO]^+$ to Fe^{2+} sites during the NO oxidation was also probed by performing the in situ Mössbauer spectroscopy. Combined with the in situ FTIR and theoretical calculations based on density functional theory (DFT), the reaction mechanism of $[FeO]^+$ sites enhances the Methanol-SCR activity by promoting the NO oxidation and generation of key intermediate HONO was revealed, which broadens the insight for low temperature Methanol-SCR catalyst design.

Results

Synthesis and characterization of Fe-FER zeolite

Fe-FER zeolites have been successfully prepared using the hydrothermal synthesis method by means of ligand-stabilized metallic species precursors mixed with synthesis gel during the crystallization (Figs. S1 and S2, Table S1). Pyrrolidine is a preferred organic structure direct agent (OSDA) of FER zeolite to complex with iron ions, enabling to achieve atomically dispersion of Fe sites in crystalline zeolite. As shown in Fig. 1a, 0.6Fe-FER zeolite, as a representative sample, exhibits a typical plate-like shape of FER zeolite and no bright nanoparticles can be observed by HAADF-STEM image, despite highly dispersed Fe sites existing in the FER zeolite, as corroborated by the energy dispersive X-ray spectra (EDS) mapping images. Spherical aberration-corrected HAADF-STEM technology was exploited to further investigate the state of Fe sites. The microporous of zeolite, along with eight-membered ring channels, can be clearly visualized, and the bright spots observed at the higher accelerating current reveal the presence of atomically dispersed Fe sites in the 0.6Fe-FER zeolite. Nevertheless, highly dispersed tiny nanoparticles gradually appear as the iron content increases to 1.2 wt%. The UV−vis spectra of 1.2Fe-FER also reveal the presence of small oligomeric Fe_xO_y clusters at 346 nm, in addition to isolated Fe ion sites at 226 and 272 nm (Fig. S3)[21]. X-ray absorption near edge structure (XANES) of Fe K-edge for the samples with Fe contents of 0.4, 0.6 and 1.2 wt% are closer to that of the reference Fe_2O_3, suggesting that Fe^{3+} is the major component in Fe-FER zeolites (Fig. 1b). Although linear combination analysis (LCA) of XANES spectra is a straightforward and widely used method in catalysis for estimating the Fe^{3+}/Fe^{2+} ratio, the use of well defined reference compounds such as bulk oxides as standards often fails to accurately replicate the XANES features of actual catalyst samples due to differences in local coordination environments. The pre-edge peak in the spectra corresponds to the dipole-forbidden 1 s → 3 d transition. The position of the pre-edge peak can also be used as a direct measure of the Fe oxidation state, making an unambiguous distinction between Fe^{2+} (~7112.5 eV) and Fe^{3+} (~7113.5 eV). Graphical analysis of the correlation between integrated intensities and positions of pre-edge features in the variogram was employed to further discriminate various oxidation states and coordination environments of Fe. Since the 1 s → 3 d transition is a quadrupolar transition, it exhibits weak intensity in coordination geometries with an inversion center (centrosymmetric geometry), such as octahedral coordination. But in fivefold or fourfold geometry, 3d−4p orbital hybridization facilitates dipole-allowed 1 s → 4p transitions, resulting in significantly higher intensity[22]. As shown in Fig. 1c and Fig. 1d, the higher integrated intensities of Fe-FER zeolites pre-edge analysis than Fe^{3+}_{Oh}, indicating that Fe sites in a lower geometry in Fe-FER zeolites than the bulk α-Fe_2O_3. The Fe^{3+}/Fe^{2+} ratio obtained by curve fitting analysis of pre-edge peak in Fe-FER zeolites exhibits an increasing trend with increasing iron loading (Table S2). It can also be demonstrated in the phase-uncorrected Fourier transform X-ray absorption fine structure (FT-EXAFS) spectra that the first contribution of Fe-FER zeolites is closer to the Fe-O scattering path and the absence of the second contribution demonstrates that Fe sites are highly dispersed in FER-zeolites in the form of coordination with oxygen (Fig. S4). According to curve-fitting results as shown in Table S3, the average distance and coordination number of Fe-O for 0.6Fe-FER zeolite are estimated to be 2.05 Å and 4.7, respectively, which are consistent with the results of pre-edge analysis. Although the

https://doi.org/10.1038/s41467-025-67458-1

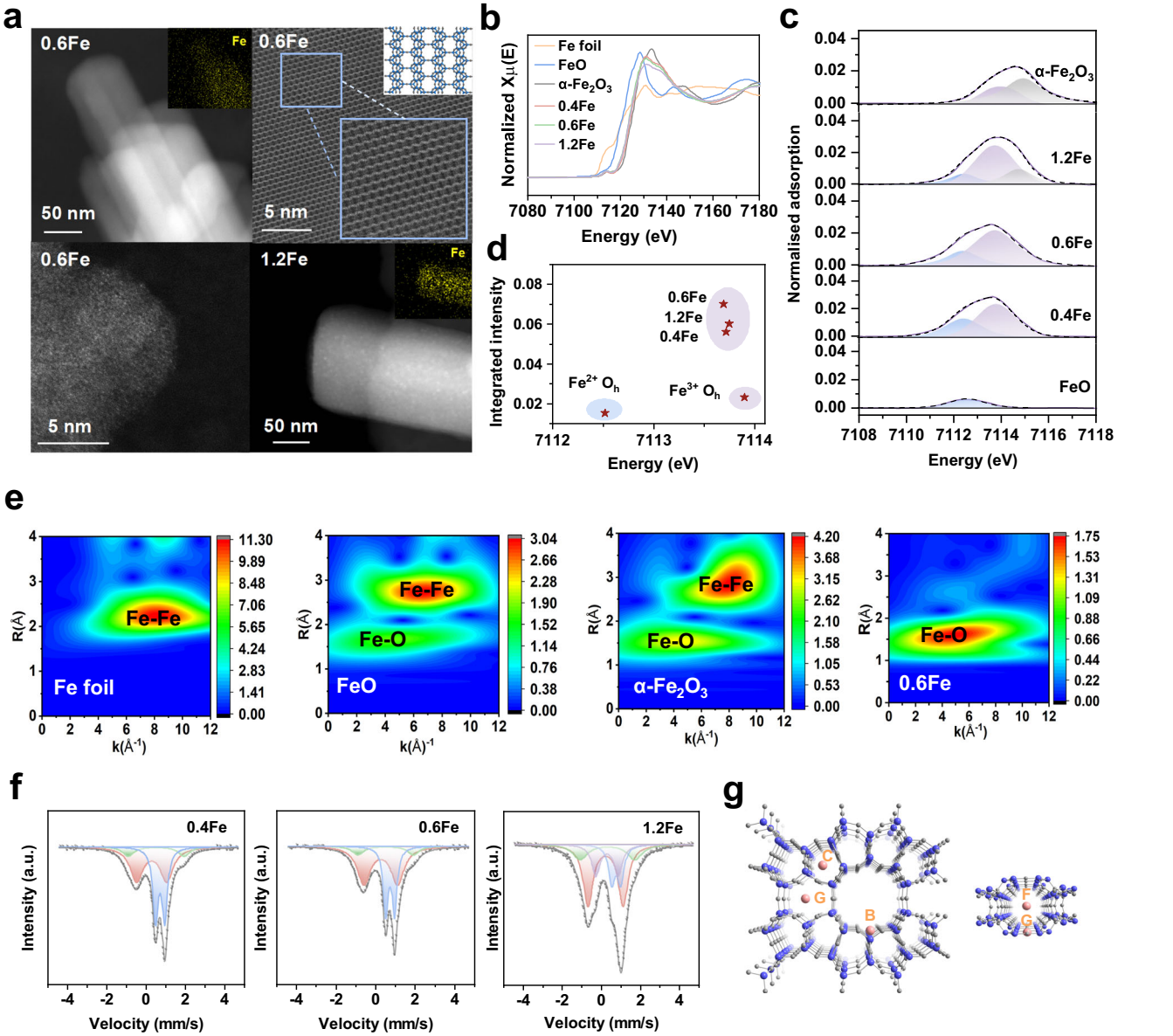

Fig. 1 | The geometric configurations and atomic compositions of Fe sites in FER zeolite. a HAADF-STEM and spherical aberration-corrected HAADF-STEM images of 0.6Fe-FER zeolite, as well as HAADF-STEM image of 1.2Fe-FER zeolite. **b** XANES spectra of Fe-FER zeolites with Fe foil, FeO, and α-Fe_2O_3 as references. **c** Pre-edge spectra of Fe-FER zeolites with FeO and α-Fe_2O_3 as references. The fitted peaks in blue and purple represent Fe^{2+} and Fe^{3+}, respectively. A distinctive feature of the pre-edge spectrum of bulk α-Fe_2O_3 is the contribution at approximately 7115 eV (shown in light grey), which is attributed to non-local transitions into the orbitals of nearest-neighbor Fe atoms. **d** Variogram of the integrated intensity and centroid position of the pre-edge peak of the Fe-FER zeolites. **e** Wavelet transform spectra of Fe foil, FeO, α-Fe_2O_3, and 0.6Fe-FER. **f** Mössbauer spectra collected at 300 °C of 0.4Fe-FER, 0.6Fe-FER, and 1.2Fe-FER zeolites. The fitted peaks in red, green, blue and purple represent component I, component II, component III, and component IV, respectively. **g** Position of B-, C-, F- and G-site in the extra-framework of FER zeolite, looking along the ten-ring channels (left) and the eight-ring channels (right).

Fe–O–Fe peaks are clearly observed in α-Fe_2O_3, they are difficult to detect in the second-shell contributions of zeolite catalysts when the metal species or oxide particles are very small and highly dispersed[23]. As for the FT-EXAFS spectra of 1.2Fe-FER, similarly, the absence of the second contribution can also be perceived, demonstrating that although the presence of nanoparticles in 1.2Fe-FER, they are still highly dispersed as iron oxide nanoparticles without any apparent agglomeration. Moreover, the absence of higher R-space signals by the wavelet transform analysis also validates the high dispersion of Fe sites (Fig. 1e and Fig. S5).

Mössbauer spectroscopy is an effective technique to provide reliable information on the forms of iron sites and the environment where iron ions exist in zeolite by measuring the hyperfine interaction between nuclear moments and electromagnetic fields[24]. Consequently, Mössbauer spectroscopy was further employed to precisely characterize the Fe sites in ^{57}Fe-FER zeolites. Mössbauer spectra are shown in Fig. 1f, and the corresponding Mössbauer parameters are listed in Table 1. The species and locations of iron can be pinpointed by the hyperfine parameters of isomer shift (IS) and quadrupole splitting (QS). Typically, $0.1 \le IS < 0.6$ mm/s and $0.6 \le IS \le 1.4$ mm/s are assignable to Fe^{3+} and Fe^{2+} component, respectively[25]. The value of QS is correlated with symmetry. Larger QS values represent the worse symmetry around iron ions[26]. As shown in Table 1, the spectral contributions of Fe-FER samples advocate that Fe^{3+} is the major

Table 1 | Mössbauer parameters, spectral contributions, and Fe sites amounts of Fe-FER zeolites

Sample	Component	IS	QS	Spectral contribution	Fe sites	Fe sites amount* / (wt%)
0.4Fe-FER	I	0.28	1.53	47%	$[FeO]^+$	0.19
	II	0.52	2.83	12%	Fe^{3+}	0.05
	III	0.72	0.47	41%	Fe^{2+}	0.16
0.6Fe-FER	I	0.25	1.70	53%	$[FeO]^+$	0.32
	II	0.50	2.80	11%	Fe^{3+}	0.07
	III	0.73	0.45	36%	Fe^{2+}	0.22
1.2Fe-FER	I	0.23	1.73	45%	$[FeO]^+$	0.54
	II	0.40	2.60	17%	Fe^{3+}	0.20
	III	0.75	0.46	18%	Fe^{2+}	0.22
	IV	0.30	1.10	20%	Small Fe_xO_y	0.24

*The amounts of Fe sites were obtained by multiplying the spectral contribution and the total iron content determined by ICP.

component in Fe-FER zeolites. Concomitantly, based on the results of ^{27}Si MAS NMR and ^{27}Al MAS NMR, the introduction of Fe^{3+} has no effect on the framework of zeolite, indicating that Fe^{3+} is primarily in the extra-framework of zeolite (Fig. S6). FER zeolite comprises ten-membered ring channels (4.2 × 5.4 Å) intersected by eight-membered ring channels (3.5 × 4.8 Å)[20]. As depicted in Fig. 1g, four characteristic positions denoted as B, C, F, and G can be occupied by isolated cations in FER zeolite as reported in previous literatures and the C-sites remain unoccupied at low iron concentration[27].

Three kinds of iron sites were found to be present in the 0.4Fe-FER and 0.6Fe-FER zeolites. The component I of 0.4Fe-FER zeolite with IS = 0.28 mm/s and QS = 1.53 mm/s and 0.6Fe-FER zeolite with IS = 0.25 mm/s and QS = 1.7 mm/s can be assigned to the $[FeO]^+$ at the six-membered ring (G-site)[28]. The component II of 0.4Fe-FER zeolite with IS = 0.52 mm/s and QS = 2.83 mm/s and 0.6Fe-FER zeolite with IS = 0.5 mm/s and QS = 2.8 mm/s has a high value of QS, suggesting that the component is in a position that confers it less symmetry. Accordingly, the Fe^{3+} at the B-site can be assigned to the component II, as reported previously[27,29,30]. The component III of the Fe-FER zeolites with IS > 0.6 mm/s is assigned to Fe^{2+}, while the lower value of QS (< 0.5 mm/s) indicates that Fe^{2+} is most likely located at the G-site and stabilized with the negative charge provided by the two aluminum. Compared to 0.4Fe- and 0.6Fe-FER zeolite, the component IV with IS = 0.30 mm/s and QS = 1.10 mm/s was observed in the 1.2Fe-FER zeolite, which is assignable to the tiny Fe_xO_y nanoparticles in accordance with the results of TEM and the reference. Collectively, single Fe^{3+} sites consist mainly of $[FeO]^+$ at G-sites and Fe^{3+} at B-sites in Fe-FER zeolites, whereas tiny Fe_xO_y nanoparticles appear as the Fe content increases to 1.2 wt%. The perturbed T-O-T vibrational modes (1000 ~ 800 cm^{-1} in the IR spectra) of the zeolite framework also provide an effective method to distinguish different Fe sites. The IR bands at 903, 895, 885, and 873 cm^{-1} are attributed to T-O-T oxygen bridges perturbed by Fe^{2+}, Fe^{3+}, $[FeO]^+$, and small oligomeric Fe_xO_y clusters, respectively (Fig. S7)[31,32]. The quantitative results are in good agreement with those obtained from the Mössbauer spectra (Table S4).

The exploitation of 2D ^1H-^1H DQ MAS NMR spectroscopy has enriched the material characterization methods at the atomic scale, allowing for in-depth exploration of the proximity between active sites, which has often been interpreted as 'the closer the better' for locating metal and acid sites[17,33]. Two off-diagonal cross-peak pairs at (4.0, 6.7) and (2.7, 6.7) ppm, as well as (2.9, 5.4) and (2.5, 5.4) ppm corresponding to the adjacent Si-O(H)-Al sites (BASs) and EFAL species (Al-OH) can be distinguished in H-FER zeolite, in addition to the diagonal autocorrelation peaks corresponding to close proximity of Si-O(H)-Al sites at (3.9, 7.8) ppm and silanols at (1.7, 3.4) ppm (Fig. 2a)[19]. The absence of autocorrelation peak at (3.9, 7.8) ppm in Fe-FER zeolites regardless of the amount of iron as shown in Fig. 2b–d suggests that Fe sites prefer to occupy one of the adjacent Si-O(H)-Al sites, resulting in the disappearance of autocorrelation peaks of BASs, as depicted in Fig. 2e. The reduced amount of BASs and enhanced amount of LASs in Fe-FER zeolites quantified by the FT-IR spectra of NH_3 adsorption also confirm that Fe sites, substituting proton countercations, exhibit Lewis acid properties by acting as electron pair acceptors[34]. The amounts of BASs determined by the $Al_{framework}$ sites are consistent with the results obtained from the FT-IR spectra of NH_3 adsorption (Fig. S8 and Fig. S9). Moreover, the content of Si-O(H)-Al sites at 3.9 ppm decreases 54% to 20% as the iron content increases in ^1H MAS NMR results and the reduction of desorption band at 300 ~ 600 °C measured by temperature-programmed desorption of NH_3 (NH_3-TPD) experiment also suggesting that Si-O(H)-Al sites are partially occupied by Fe sites (Fig. S10, Table S5 and Fig. S11)[35]. No significant difference is observed before 650 °C between the TCD and MS signals, indicating that ammonia decomposition does not occur in Fe-FER zeolites. The BASs formed by framework aluminum in zeolites are primarily located within the internal channels. The introduction of iron species mainly exists as ion sites that replace BASs and are incorporated into the zeolite channels. In contrast, EFAL species are also distributed on the external surface of the zeolite. Therefore, the introduction of iron has a more significant impact on the BASs compared to the EFAL species.

Catalytic performance of Fe-FER zeolites

Since the excellent redox properties are crucial for the SCR reaction, the NO oxidation performance of the Fe-FER zeolites was first investigated[36,37]. The conversion of NO increases gradually can be observed with the increment of iron content and the activation energy for NO oxidation of the 0.6Fe-FER zeolite (E_a=31.2 kJ/mol) is lower than that of the H-FER zeolite (E_a=56.6 kJ/mol), suggesting that the introduction of Fe sites is conducive to the oxidation of NO (Fig. 3a and S12). Concomitantly, investigations were steered towards the correlation between the content of different Fe sites and the reaction rate of NO oxidation. The reaction rates for NO oxidation, which excludes the limitations of internal and external diffusion, manifest an immensely good linear relationship with the amount of $[FeO]^+$ present in Fe-FER zeolites (Fig. 3b). On the contrary, neither the amount of the Fe^{3+} nor the Fe^{2+} correlates with the reaction rate of NO (Fig. S13). Reaction order with respect to NO was measured over the 0.6Fe-FER zeolite by analyzing the reaction rate dependency on reactant concentration. As shown in Fig. S14, the reaction rate was found to have linear dependence with respect to NO, with the slope of the linear fit being approximately 1, indicating that the reaction follows first-order kinetics.

In situ Mössbauer and FT-IR spectroscopy were employed to monitor the changes of Fe sites during the NO oxidation reaction.

https://doi.org/10.1038/s41467-025-67458-1

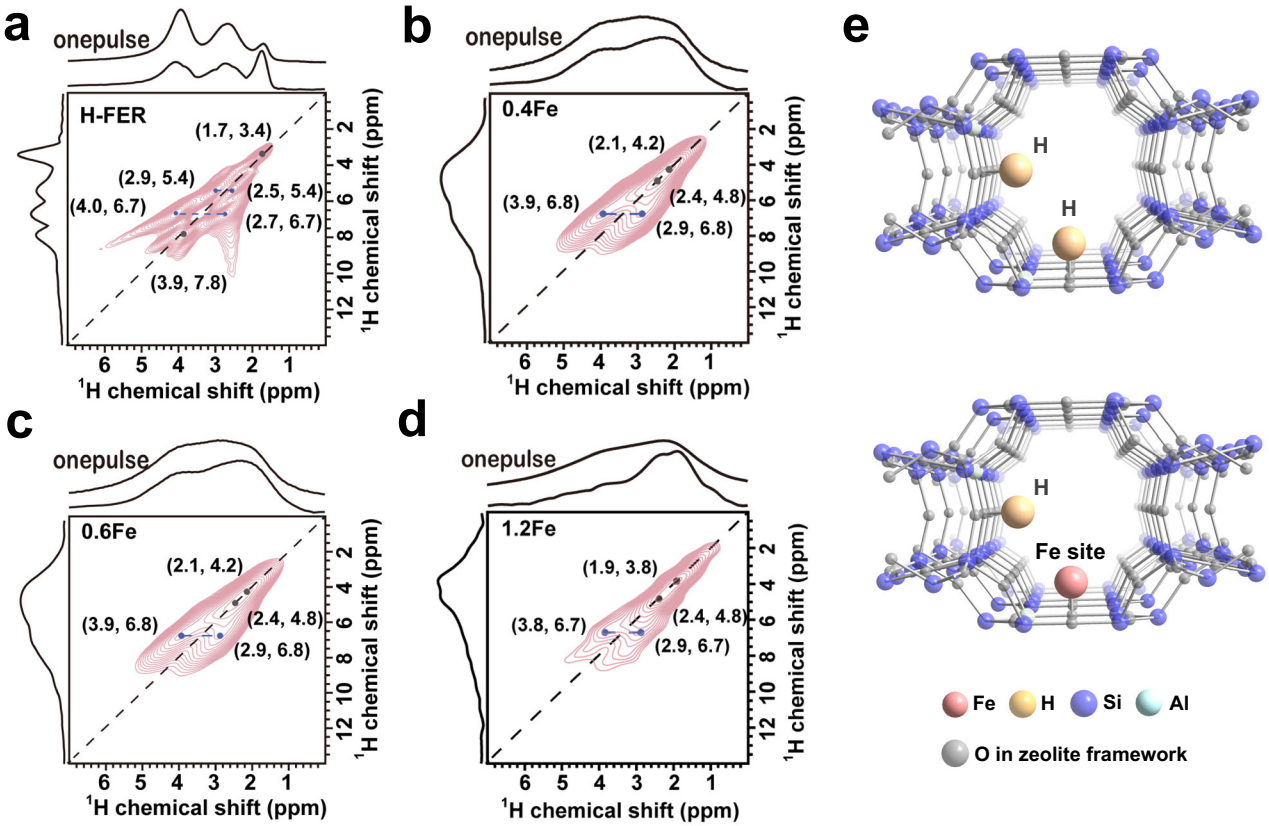

Fig. 2 | 2D ^{1}H-^{1}H DQ MAS NMR characterization of the Fe site location in FER zeolite. 2D ^{1}H-^{1}H DQ MAS NMR spectra of (**a**) H-FER, **b** 0.4Fe-FER, **c** 0.6Fe-FER and **d** 1.2Fe-FER zeolites. **e** Structural schematic of the adjacent Si-O(H)-Al sites and one of the adjacent Si-O(H)-Al sites occupied by single-atom Fe sites.

Mössbauer spectra are shown in Fig. 3c and the corresponding Mössbauer parameters are listed in Table 2. Firstly, the catalyst was oxidized under the reaction atmosphere of 14% O_2/N_2. With the introduction of 1000 ppm NO/N_2, the content of component I decreases from 53% to 10%, accompanied by the appearance of a Fe^{2+} site (component V), signifying that the $[FeO]^+$ was reduced to Fe^{2+}. Compared to component I, the insignificant change in QS values of component V points to the $[Fe^{2+}\text{-}NO_2^-]^+$ structure may be formed at the G-site. When 14% O_2/N_2 was introduced instead of NO, the oxidation reaction from Fe^{2+} to $[FeO]^+$ took place according to the disappearance of component V in conjunction with the component I increasing from 10% to 52%. Time-resolved in situ FT-IR spectra on 0.6Fe-FER zeolite were also employed as a complementary technique to monitor changes in Fe sites during the NO oxidation reaction (Fig. 3d). The introduction of 1000 ppm NO/N_2 induced a distinct shift of the T–O–T vibrational peak to higher wavenumbers in IR spectra, suggesting increased formation of Fe^{2+} species with a significant decrease in the $[FeO]^+$ site. This shift is accompanied by the emergence of IR bands at 1870, 1590, and 1478 cm^{-1}, which are attributed to Fe^{2+}–NO, nitrates, and Fe^{2+}–NO_2^- species, respectively. Accordingly, the IR band at 909 cm^{-1} can be assigned to T–O–T oxygen bridges perturbed by Fe^{2+}–NO_2^- species. When 14% O_2/N_2 was introduced instead of NO, a time-dependent shift of the T–O–T vibrational peak to lower wavenumbers was observed, accompanied by the appearance of a band at 1625 cm^{-1} (attributed to NO_2 adsorption) and a decrease in the Fe^{2+}–NO_2^- species at 1478 cm^{-1}. These observations suggest that NO oxidation proceeds via Fe^{2+}–NO_2^- as an intermediate, as depicted in Fig. 3e, which is in good agreement with the results of the Mössbauer spectra. The significant variance observed in $[FeO]^+$ demonstrates its pivotal role as an active site in the NO oxidation reaction. The $[FeO]^+$ site can react with NO to form $[Fe^{2+}\text{-}NO_2^-]^+$ intermediate. Subsequently, NO_2 is generated via electron transfer from NO_2^- to the oxygen atom (originating from O_2), forming the $[Fe^{2+}\text{-}O^-]^+$ intermediate. Further electron transfer from Fe^{2+} to O^- facilitates the formation of $[FeO]^+$. Time-resolved in situ FT-IR experiment was also conducted to investigate the influence of methanol on Fe sites under reaction conditions. As shown in Fig. S15, the introduction of methanol causes no noticeable change in the perturbed T–O–T vibration of Fe sites, implying that methanol exerts a negligible influence on the iron sites under the reaction conditions.

Methanol-SCR activities were investigated on H-FER zeolite and a series of Fe-FER zeolites. As shown in Fig. 4a, Fe-FER zeolites significantly enhance the catalytic activity at low temperature region (250-350 °C) in comparison with H-FER zeolite. With the increasing Fe content up to 0.6 wt%, the conversion rate of NO_x at the low temperature region increases gradually with the optimal reaction temperature for the maximum NO_x conversion (T_{max}) shifting down to a lower temperature (350-300 °C), as shown in Fig. S16. When the Fe content exceeded 0.6 wt%, the catalytic activities gradually decreased at all the entire temperature range (Fig. S17). The decrease in the conversion rate of NO_x on Fe-FER zeolites at high temperature (>300 °C) can be ascribed to the oxidation of methanol to CO and CO_2, which leads to a shortage of the reductant for the Methanol-SCR reaction, as corroborated by the reaction of methanol oxidation in the absence of NO_x in Fig. S18. It is noteworthy that Fe-FER zeolite with high iron content (e. g. 1.2 wt%) is more likely to oxidize methanol to CO_2 due to the presence of iron oxide nanoparticles[38]. Meanwhile, under the optimum reaction temperature window (225 - 300 °C), 0.6Fe-FER zeolite exhibits the best yield of N_2, accompanied by the least N_2O formation, as illustrated in Figs. S19 and S20. A progressive increase in iron content leads to a corresponding decline in both deNO_x activity and N_2 selectivity during the Methanol-SCR reaction, primarily owing to the loss of BASs in the catalysts, as BASs have been

https://doi.org/10.1038/s41467-025-67458-1

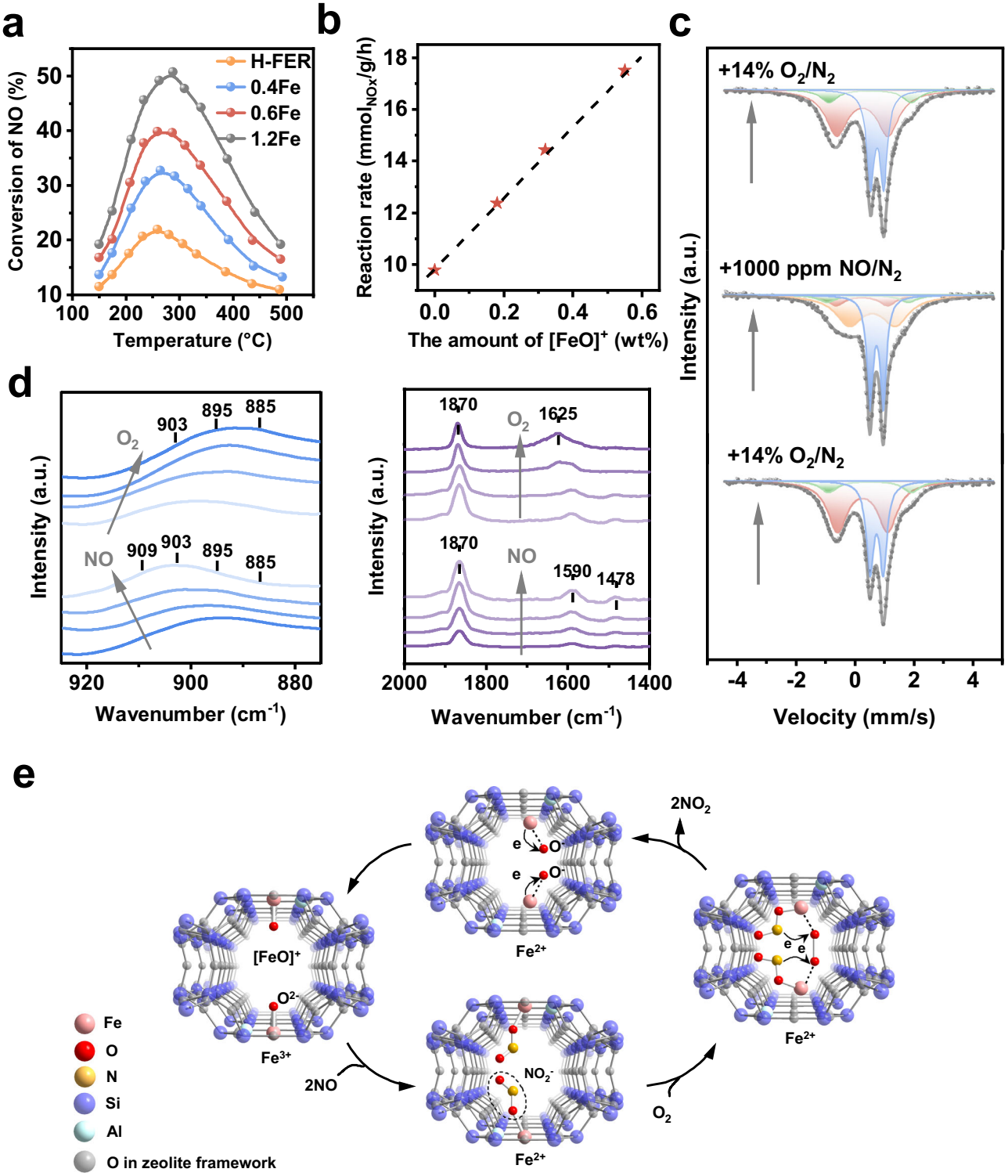

Fig. 3 | The dynamic evolution of Fe sites during the NO oxidation reaction. **a** Effect of the amount of Fe on the activity of NO oxidation on FER zeolites. **b** The relationship of the amount of $[FeO]^+$ with reaction rate for NO oxidation at 175 °C. **c** In situ Mössbauer spectra of 0.6Fe-FER zeolite were collected at 300 °C with 14% O_2/N_2 flowed in; with 1000 ppm NO/N_2 flowed in instead of 14% O_2/N_2; with 14% O_2/N_2 flowed in instead of 1000 ppm NO/N_2. The arrows represent the order in which the gases were introduced. The fitted peaks in orange represent the component V. **d** Time-resolved in situ FT-IR spectra of 0.6Fe-FER zeolite collected at 300 °C with 14% O_2/N_2 flowed in; with 1000 ppm NO/N_2 flowed in instead of 14% O_2/N_2; with 14% O_2/N_2 flowed in instead of 1000 ppm NO/N_2. The spectra were collected with 1-minute intervals. **e** Structural schematic of the dynamic evolution of Fe sites during the NO oxidation reaction.

reported to be closely associated with the high temperature activity and N_2 selectivity in Methanol-SCR reactions (Fig. S21)[20]. Moreover, the Fe-FER zeolites exhibit a competitive advantage in low-temperature deNO_x efficiency compared to other Methanol-SCR catalysts, such as the reported Ag/Ag_2O_3 and Cu-containing catalysts (Figs. S22, S23 and Table S6). The products derived from methanol were also analyzed, as shown in Fig. 4b. Dimethyl ether was readily formed at low temperature (<250 °C) and a small amount of formaldehyde was also detected

https://doi.org/10.1038/s41467-025-67458-1

Table 2 | Mössbauer parameters, spectral contributions, and Fe sites amounts of 0.6Fe-FER zeolites under different reaction atmospheres at 300 °C

Sample	Component	IS	QS	Spectral contribution	Fe sites	Fe sites amount* / (wt%)
+14% O_2/N_2	I	0.25	1.70	53%	$[FeO]^+$	0.32
	II	0.50	2.80	11%	Fe^{3+}	0.07
	III	0.73	0.45	36%	Fe^{2+}	0.21
+1000 ppm NO/N_2	I	0.23	1.75	10%	$[FeO]^+$	0.06
	II	0.43	2.75	7%	Fe^{3+}	0.04
	III	0.73	0.45	38%	Fe^{2+}	0.23
	V	0.78	1.56	45%	Fe^{2+}	0.27
+14% O_2/N_2	I	0.24	1.73	52%	$[FeO]^+$	0.31
	II	0.49	2.78	12%	Fe^{3+}	0.07
	III	0.73	0.44	36%	Fe^{2+}	0.22

*The amounts of Fe sites were obtained by multiplying the spectral contribution and the total iron content determined by ICP.

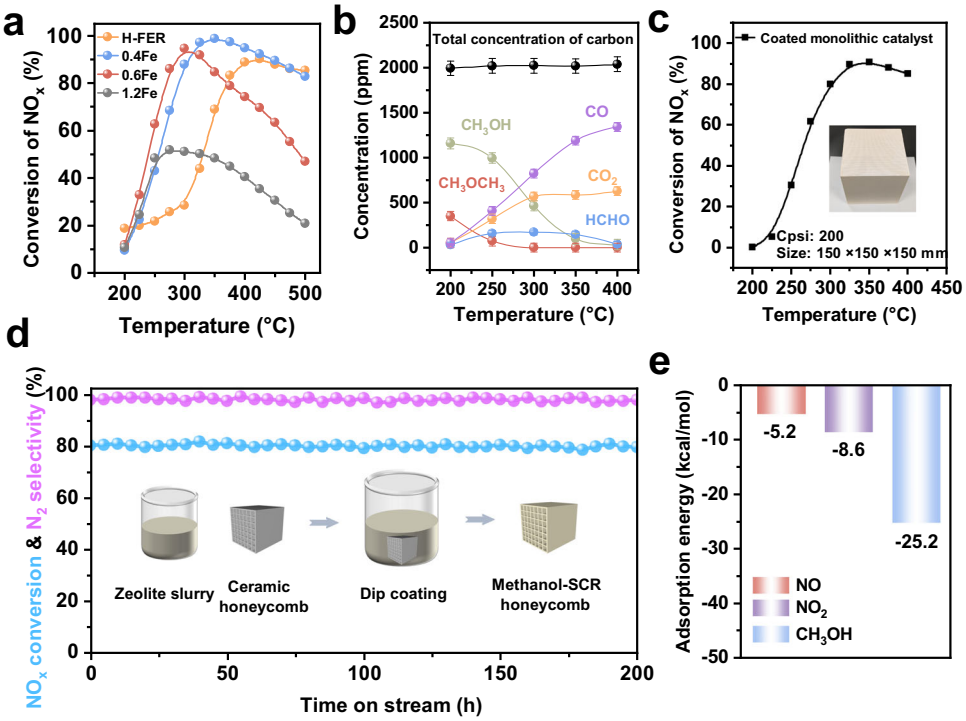

Fig. 4 | Catalytic performance of Fe-FER zeolites in Methanol-SCR reaction. **a** Effect of the amount of Fe on NO_x conversion for Methanol-SCR on FER zeolites. **b** The conversion of methanol in Methanol-SCR on 0.6Fe-FER zeolite. Error bars indicate the standard deviation from at least three independent measurements. **c** The bench test of the monolithic catalyst coated with 0.6Fe-FER zeolite. **d** The catalytic stability of the coated monolithic catalyst at 300 °C and simplified representation of the integrated honeycomb ceramic catalyst (inset picture). **e** The calculated adsorption energies of NO, NO_2, and CH_3OH molecules on BAS in the FER zeolite.

as by-products in addition to CO and CO_2. Compared with the serious deactivation of NH_3-SCR catalysts such as commercial $V/W/TiO_2$ and Cu-CHA, 0.6Fe-FER zeolite shows only <5% loss of activity at the low temperature region (<300 °C) after withstanding the same SO_2 poisoning treatment as that reported for $V/W/TiO_2$ catalyst, while the activity at high temperature region (>300 °C) is virtually unaffected (Fig. S24)[39,40]. For potential industrial application, the bench test was also conducted under the reaction condition simulating methanol engine exhaust, using a 150 × 150 × 150 mm monolithic catalyst coated with 0.6Fe-FER zeolite (Figs. S25 and S26). As shown in Fig. 4c, the coated monolithic catalyst still remains higher catalytic activity, achieving NO_x conversion above 80% within the temperature range of 300 to 400 °C, and a remarkable catalytic stability with more than 200 h could also be achieved at 300 °C (Fig. 4d).

The activation of methanol in zeolite to form methyl groups plays a strikingly important role in the Methanol-SCR reaction on the basis of our previous work[20]. As displayed in Fig. S27, when CH_3OH and O_2 were introduced, three identical methyl signals at 60.9, 59.2 and 50.5 ppm are observed on both H-FER and 0.6-Fe-FER zeolites corresponding to side-on adsorbed dimethyl ether (DME), methyl groups generated on BAS and adsorbed methanol, respectively[41]. No new methyl signals appeared on 0.6Fe-FER zeolite, signifying that methanol is mainly activated on BASs rather than Fe sites. The adsorption capacity of NO, NO_2 and CH_3OH molecules on BASs was also explored by DFT calculations. It reveals that the BASs in FER zeolite display a much stronger adsorption capacity for CH_3OH molecules (25.2 kcal/mol) than that for NO (5.2 kcal/mol) and NO_2 (8.6 kcal/mol), as manifested in Figs. 4e and S28. Together

https://doi.org/10.1038/s41467-025-67458-1

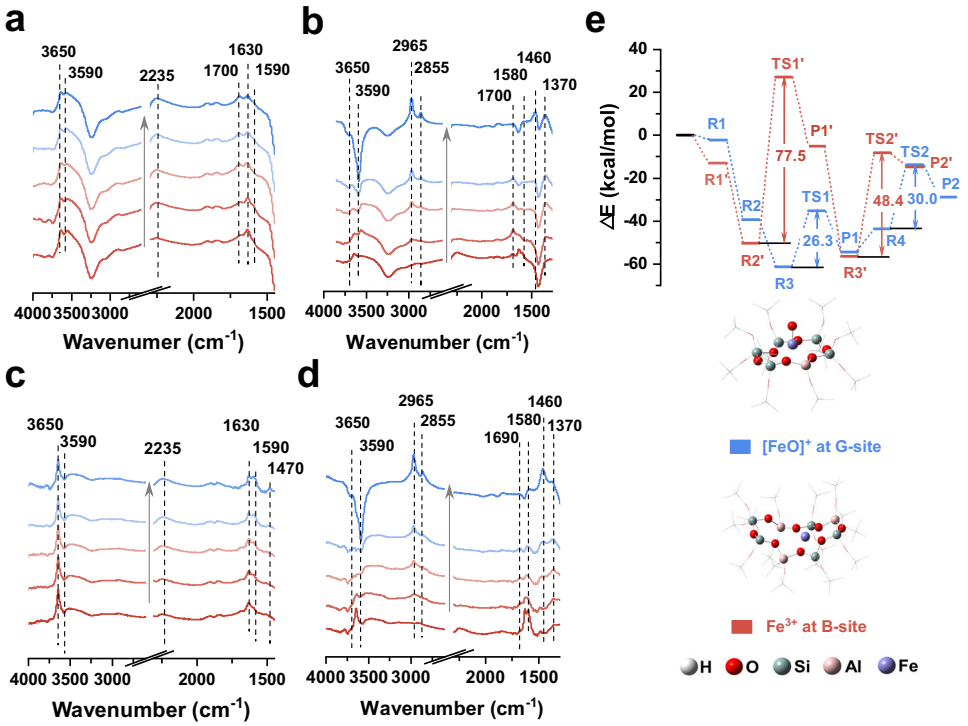

Fig. 5 | The role of Fe sites in Methanol-SCR reaction. Time-resolved in situ FT-IR spectra on H-FER zeolite with (**a**) 500 ppm NO and 7% O_2 flowed in at 300 °C for 30 min; **b** 1000 ppm CH_3OH and 7% O_2 flowed in at 300 °C for 30 min after 500 ppm NO flowed in at 300 °C for 30 min. Time-resolved in situ FT-IR spectra on 0.6Fe-FER zeolite with (**c**) 500 ppm NO and 7% O_2 flowed in at 300 °C for 30 min; **d** 1000 ppm CH_3OH and 7% O_2 flowed in at 300 °C for 30 min after 500 ppm NO flowed in at 300 °C for 30 min. H_2O was introduced by bubbling with N_2 (1 mL/min) at 30 °C during all of the tests for the simulation of Methanol-SCR reaction with the co-existence of H_2O. **e** Comparison of reaction energy barrier for the formation of HONO on $[FeO]^+$ at G-site and Fe^{3+} at B-site in FER zeolite.

with the results of ^{13}C CP/MAS NMR measurements as illustrated in Fig. S27, it can be reasonably inferred that the BASs will be preferentially occupied by the methanol molecules and further activated to form methyl groups during the Methanol-SCR reaction. An explanation can also be given that the decrease in the activity on Fe-FER zeolites with higher iron content (>0.6 wt%) is most likely owing to the massive absence of BASs where methanol is activated. The methanol outlet concentrations during the Methanol-SCR reaction over 0.6Fe-FER and 1.2Fe-FER zeolites are shown in Fig. S29. At temperatures below 300 °C, the methanol outlet concentration of 1.2Fe-FER is higher than that of 0.6Fe-FER. Given that methanol oxidation does not occur below 300 °C (Fig. S18), the lower activity of 1.2Fe-FER is attributed predominantly to the reduced BAS rather than methanol consumption via oxidation. However, the decrease in NO_x conversion over Fe-FER zeolites at high temperature (>300 °C) can be influenced by both the loss of BASs and the oxidation of methanol. Increasing the CH_3OH inlet concentration enhances Methanol-SCR activity at high temperatures (>300 °C), further supporting this speculation that the oxidation of methanol to CO and CO_2 may leads to a shortage of the reductant for Methanol-SCR reaction (Figure S30). To ensure similar CH_3OH outlet concentrations, the reaction rates were measured for 0.6Fe-FER with a CH_3OH inlet concentration of 3500 ppm and for 1.2Fe-FER with a CH_3OH inlet concentration of 3000 ppm at temperatures below 300 °C. At temperatures above 300 °C, the reaction rates were determined for 0.6Fe-FER with a CH_3OH inlet concentration of 3500 ppm and for 1.2Fe-FER with a CH_3OH inlet concentration of 4000 ppm. Although the CH_3OH outlet concentration remained similar, the 0.6Fe-FER zeolite still exhibits a higher reaction rate than the 1.2Fe-FER zeolite, indicating that even under conditions of sufficient reductant availability, the loss of BASs substantially impairs Methanol-SCR activity over the entire temperature range (Fig. S31).

The role of Fe sites in Methanol-SCR reaction

In practical SCR reactions, the abundant presence of water vapor inevitably facilitates the interaction of NO_x with H_2O, thereby leading to the formation of nitrites or nitrates that act as reactive intermediates in the overall process. In both NH_3-SCR and Methanol-SCR processes, HONO has been identified as a crucial nitrogen-containing reaction intermediate, and its formation is also influenced by the NO/NO_2 ratio. Therefore, the formation of HONO on the catalysts was further investigated. Time-resolved in situ Fourier transform infrared (FT-IR) experiments were implemented to further reveal the effect of Fe sites on Methanol-SCR reaction. As shown in Fig. 5a, when NO and O_2 were flowed in, the adsorbed NO_2 (1630 cm^{-1}) was first observed on H-FER zeolite; meanwhile, the adsorbed nitrates (1590 cm^{-1}), N_2O_3 (1700 cm^{-1}), and NO^+NO_2 (2235 cm^{-1}) species appeared gradually[42–44]. Subsequently, CH_3OH was introduced in place of NO, and absorption peaks at 1370, 1460, 2855, and 2965 cm^{-1} corresponding to methyl groups appeared, accompanied by the consumption of absorption peaks at 3590 cm^{-1} and 3650 cm^{-1}, owing to the absorption and activation of methanol on BAS and EFAL species (Al-OH), respectively (Fig. 5b)[45]. Compared to H-FER zeolite, 0.6Fe-FER zeolite exhibits different adsorption species when NO and O_2 are flowed in. As shown in Fig. 5c, no adsorbed N_2O_3 species were observed on the 0.6Fe-FER zeolite, while the formation of nitrite (1470 cm^{-1}) was detected[46]. HONO has been proposed as a key intermediate in the SCR reaction over both copper- and iron-containing zeolites, and is also regarded as a nitrite-precursor. However, it is difficult to detect directly as a highly reactive intermediate. Once formed, it is rapidly adsorbed by hydroxyl groups and subsequently converted into nitrite species via reactions such as Al–OH + HONO → Al–ONO + H_2O. Therefore, nitrite species are generally accepted as indirect evidence for the formation of HONO. In the Methanol-SCR reaction, HONO produced by the interaction of NO_x with H_2O corresponds to a general reaction occurring on zeolites:

$NO + NO_2 + H_2O \rightarrow 2HONO$. In comparison, under dry conditions, more NO^+NO_2 and adsorbed NO_2 species were formed on the 0.6Fe-FER zeolite, whereas the adsorbed NO_2 species were not further converted to HONO, as shown in Fig. S32. As the purging process commences, the hydroxyl vibration at ~3650 cm^{-1} rapidly disappears, whereas the IR absorption band at 1630 cm^{-1} remains, suggesting that the species responsible for the IR absorption band at 1630 cm^{-1} is primarily adsorbed NO_2 rather than water. Accordingly, the absence of H_2O leads to a significant decrease in Methanol-SCR reactivity (Fig. S33).

Furthermore, when CH_3OH was introduced instead of NO, the generation and consumption of IR absorption band at 1690 cm^{-1} can be captured, as manifested in Fig. 5d. Notably, the species with the IR absorption band at 1690 cm^{-1} is assigned to formamide, another key intermediate in the Methanol-SCR reaction, which can be formed by the conversion of nitromethane resulting from the reaction of methyl groups and adsorbed HONO[19,20,47]. These reaction intermediates are consistent with those previously reported for the Methanol-SCR process[19]. With the aid of SVUV-PIMS spectroscopy, Chen et al. found the presence of nitromethane but with a low ion signal strength in the Ethanol-SCR and (NH_3+Ethanol)-SCR processes[48]. The above elaboration points to the fact that the introduction of Fe sites not only facilitates the oxidation of NO, but also further promotes the generation of the key intermediate HONO, thus enhancing the reactivity of Methanol-SCR. A comprehensive reaction pathway for the Methanol-SCR process was proposed, as depicted in Fig. S34. BASs contribute to the adsorption and activation of methanol to generate active methyl groups, while $[FeO]^+$ sites are conductive to produce HONO, thereby accelerating the generation of the key intermediate nitromethane, which can transform to formamide and subsequently react with NO_x to produce N_2.

Since the component III of Fe^{2+} at G-site is insensitive to oxidizing and reducing treatment and shows little tendency to participate in the reaction, DFT calculations were adopted to further explore the role of Fe^{3+} and $[FeO]^+$ sites in the formation of HONO. According to the results of Mössbauer spectra, the models of $[FeO]^+$ at the G-site and Fe^{3+} at the B-site are constructed in FER zeolite, and the reaction pathways for generating HONO are proposed, as depicted in Fig. S35. On the $[FeO]^+$ at G-site, NO first reacts with $[FeO]^+$ to form Fe^{2+}-NO_2^-, then NO_2^- reacts with H_2O to produce Fe-OH and a HONO with an energy barrier of 26.3 kcal/mol. Afterwards, the Fe-OH should overcome a barrier of 30 kcal/mol, and react with NO_2 to form $[FeO]^+$ and another HONO. The reaction path follows a general reaction in zeolite: $NO + NO_2 + H_2O \rightarrow 2HONO$. On the Fe^{3+} at the B-site, NO_2 is more likely to adsorb on the Fe^{3+} site first, and a prohibitively high energy barrier (77.5 kcal/mol) needs to be overcome to generate HONO (Fig. 5e). The above results suggest that $[FeO]^+$ at the G-site can function as a promoter of HONO production, whereas Fe^{3+} at the B-site does not. The formed HONO will further react with the activated methyl group at the BASs to produce the key intermediates nitromethane and formamide, thereby enhancing the catalytic performance of Methanol-SCR.

Overall, $[FeO]^+$ is a preferred active site for the NO oxidation and Methanol-SCR. The dynamic evolution of Fe sites provides an interpretation that Fe sites with reactive oxygen are susceptible to the oxidation and reduction treatment, accompanied by variation in the valence state of the Fe sites. Conversely, the respective Fe^{2+} at the G-site and Fe^{3+} at the B-site are difficult to activate during the reaction process. Notably, $[FeO]^+$ has two fewer positive charges than Fe^{3+}, so less negative charge is required to balance the $[FeO]^+$ site in the framework of zeolite, which allows more Si-O^--Al sites to be released to produce BASs. BASs also play a critical role in Methanol-SCR. On one hand, methanol can be activated on BASs to generate methyl groups to participate in the reaction. On the other hand, BASs are directly related to N_2 selectivity, as reported in the previous studies. CHA and FER zeolites with a Cu loading of 0.6 wt% were prepared and evaluated for the Methanol-SCR and NO oxidation reaction (Fig. S22). The Cu-FER zeolite prepared by the ion exchange method (0.6Cu-FER-IE) exhibits high catalytic activity in the temperature range of 350~450 °C with the conversion of NO_x above 70%, while the Cu-CHA zeolite, commonly used as a commercial NH_3-SCR catalyst, showed less than 20% activity across the entire temperature range. The catalytic performance of the Cu-FER zeolite in the Methanol-SCR reaction appears to depend primarily on the BASs of the FER framework, as its activity is similar to that of the H-FER zeolite. Moreover, neither the Cu-FER nor the Cu-CHA zeolite exhibits significant NO oxidation activity. The pronounced difference in activities between the Cu-FER zeolites synthesized by different methods suggests the presence of distinct copper species in the two catalysts, a phenomenon that needs further investigation. A methanol oxidation experiment was also conducted for the Cu-CHA zeolite. As shown in Fig. S36, in contrast to the Fe-FER zeolite, the Cu-CHA zeolite predominantly oxidizes methanol to CO_2 rather than CO, suggesting that the two catalysts exhibit markedly different behaviors in methanol oxidation. This implies that the carbon-containing intermediates formed during the Methanol-SCR process are likely different for these two catalysts. FER zeolite is a medium-pore zeolite consisting of 10-membered ring (4.2 × 5.4 Å) channels intersected by 8-membered ring (3.5 × 4.8 Å) channel, whereas the CHA zeolite features a three-dimensional microporous framework composed of cha cages interconnected by eight-membered ring (8-MR) windows (~3.8 × 3.8 Å). The low activity of the CHA zeolite in the Methanol-SCR reaction is likely attributed to its unique microporous structure, which easily causes carbon deposition during the methanol-related reaction[49]. It indicates that the zeolite topology also plays a crucial role in the Methanol-SCR catalytic performance.

In this work, we have demonstrated that the collaboration of acid sites and iron redox sites in zeolite can promote the low-temperature Methanol-SCR activity on a series of Fe-FER zeolites, which boosts the catalytic activity of Methanol-SCR significantly at low temperature region (250-350 °C). Pilot-scale bench test using the coated monolithic catalyst also exhibited a remarkable NO_x conversion and a high stability at low temperature, clearly indicating the great potential application of Fe-FER zeolite catalyst in industrial Methanol-SCR. Further mechanistic studies indicated that BASs in FER zeolite could generate methyl groups by activating methanol, whereas an atomically dispersed $[FeO]^+$ site would further improve the redox properties of the Methanol-SCR catalysts by facilitating the oxidation of NO and the generation of key intermediate HONO. This work discloses the similar design principles of SCR catalysts, and deepens the cognition and understanding of the redox sites for SCR reaction. It not only provides a powerful way to design promising Methanol-SCR catalysts, but also offers a guiding direction for the establishment of the structure-activity relationship of such SCR catalysts.

Methods

Catalyst preparation

FER zeolite catalysts were prepared by the hydrothermal method with pyrrolidine and ethylene glycol as structure-directing agents (SDAs). Firstly, 0.245 g of NaOH and 0.48 g of $NaAlO_2$ were dissolved in 10 g of H_2O. Then, 3 g of fumed silica was added to the mixture under rigorous stirring, followed by 21 g of ethylene glycol being dropped in the above solution. The obtained gel was transferred into an autoclave with a PTEE liner for hydrothermal synthesis at 180 °C for 24 h. Subsequently, a mixture prepared by ferric sulfate with different masses and 0.392 g of pyrrolidine dissolved in 3.5 g of H_2O was added to the cooled gel and continued to hydrothermal synthesis at 180 °C for 72 h. The obtained product was separated, followed by washing with deionized water, drying at 100 °C overnight. Finally, the obtained solid was calcinated in air at 600 °C for 6 h to remove the SDAs and calcined at 550 °C for 2 h followed by ion exchanging with the solution of NH_4Cl for 3 times to get Fe-FER catalysts. The final product was denoted as xFe-FER, of which the suffix of x referred to the mass percentage of the loading of

Fe. H-FER was prepared by a similar procedure except for the addition of ferric sulfate. 0.6Cu-FER-one pot zeolite was successfully synthesized using copper sulfate as the Cu precursor, following the same protocol as 0.6Fe-FER zeolite. Cu-FER-IE and Cu-CHA zeolites were prepared by ion exchanging with the solution of copper acetate. The detailed procedure is as follows: 0.031 g of copper acetate was dissolved in 10 g of H_2O, followed by the addition of 3 g of NH_4-FER or NH_4-CHA zeolite to the copper acetate solution. The mixture was stirred vigorously at 80 °C for 2 h. The resulting Cu-FER-IE or Cu-CHA sample was then obtained by filtration, washed with deionized water, dried at 100 °C overnight, and finally calcined at 550 °C for 2 h.

XRD measurement

The framework of the FER samples was confirmed by powder XRD patterns with Cu Kα radiation (λ = 1.5418 Å) and with a scan rate of 2θ = 8.0 °/min at 3- 55° (Rigaku MiniFlex 600 Benchtop X-ray diffractometer).

Inductively coupled plasma atomic emission spectroscopy (ICP-AES)

The content of Fe present in FER zeolite was determined by ICP-AES (Agilent Technology 4210).

UV-vis spectra

The UV-vis spectra were depicted with a UV-vis spectrophotometer (UV-2600, Shimadzu).

N_2 adsorption and desorption measurement

N_2 adsorption/desorption experiments of samples were performed on 3H-2000PM2 (BEISHIDE), and the samples were degassed under vacuum at 200 °C for 5 h before analysis. Typically, the Brunauer-Emmett-Teller (BET) equation was used to calculate the specific area of the sample, and the micropore specific surface area was evaluated using t-plot method.

TEM

HR-TEM, HAADF, and EDS images were taken using a FEI Talos F200X S/TEM with a field-emission gun at 200 kV. A spherical aberration-corrected HAADF-STEM image was taken by JEM-ARM300F with a field-emission gun at 300 kV. The pores of zeolite and Fe single atom were operated at the accelerating current of 5 μA and 15 μA, respectively.

XAS measurement

Fe K-edge XAS were carried out using a synchrotron radiation ring at PF-12 C beamline (Photon Factory, KEK) equipped with a Si(111) single-crystal monochromator in a fluorescence mode. The data analysis of the XAS spectra was conducted by the Demeter software package ATHENA and ARTEMIS[50]. The Fourier transform of the k^3-weighted EXAFS was carried out over a k range of 3–10 $Å^{-1}$. Samples were pretreated to remove the adsorbed water at 200 °C for 2 h in flowing synthetic air before sealing in polyethylene cells for XAS measurements.

In situ Mössbauer spectroscopy measurements

For Mössbauer spectroscopy measurements, ^{57}Fe was introduced into FER zeolites by the above-described methods. The transmission ^{57}Fe Mössbauer spectra were collected at 300 °C using ^{57}Co in Rh matrix as a source. The velocity scale was calibrated using sodium nitroprusside (SNP), and the isomer shift quoted in this work is relative to that of the α-Fe. The spectra were analyzed using the MossWinn software[51]. Prior to the Mössbauer spectra test, all the samples were dehydrated at 500 °C in 14% O_2/N_2 for 2 h. Thereafter, the reaction gas at a flow of 50 mL/min was introduced at 300 °C for 1 h in the following order: 14% O_2/N_2; 1000 ppm NO/N_2; 14% O_2/N_2).

NMR measurements

All NMR experiments were performed on a Bruker Avance III 400 MHz spectrometer with resonance frequencies of 400.1 and 100.6 MHz for ^{1}H and ^{13}C, respectively. ^{1}H MAS NMR spectra were collected at a MAS rate of 10 kHz, using a single-pulse excitation of π/2, pulse duration of 2.6 μs, and a repetition time of 20 s. 2D ^{1}H-^{1}H DQ MAS NMR experiments were executed using a POST-C7 pulse sequence with a recycle delay of 20 s and a MAS rate of 10 kHz. 16 scans were acquired for each t1 increment. Note that prior to ^{1}H NMR test, all the samples were dehydrated at 420 °C in vacuum (below 10^{-3} Pa) for 12 h. ^{13}C CP/MAS NMR spectra were collected using a 4.0 mm HX double resonance MAS NMR probe at a MAS rate of 10 kHz. A number of scans of 1800 and a repetition time of 4 s were used. The samples pelletized in 80-100 mesh were firstly pretreated at 500 °C for 2 h in synthetic air. Thereafter, the reaction gas at a flow of 50 mL/min was introduced at 300 °C $CH_3OH + O_2$ (1000 ppm $^{13}CH_3OH$ and 7% O_2 in N_2 atmosphere). Finally, the sample was quickly cooled down for ^{13}C NMR measurement.

NH_3-TPD measurements

NH_3-TPD experiments were performed on a chemisorption analyzer (PCA-1200 Builder Technology). The samples were pretreated at 400 °C for 1 h in synthetic air with a flow of 50 mL/min to remove the adsorbed water. The temperature was cooled down to 100 °C and saturated with 1% v/v NH_3/He mixture with a flow rate of 20 mL/min for 1 h. Physisorbed ammonia was removed at 100 °C for 1 h in helium flow until the TCD signal was stabilized. The sample was heated from 100 °C to 700 °C with a 5 °C/min ramping rate in a helium flow rate of 20 mL/min^{-1}. Desorption of NH_3 was monitored by mass spectrometry (m/z = 16).

In situ FT-IR spectroscopy

In situ FT-IR experiments were conducted on a Thermal Scientific Nicolet iS 10 instrument with a DTGS detector. Infrared spectra were overlapped 16 times at a resolution of 4 cm^{-1}. ~10 mg of the sample was pressed into a slice (0.8 MPa) with a diameter of 13 mm and then transferred to the transmission cell equipped with ZnSe windows. The sample was pretreated at 500 °C for 2 h with a flow of 50 mL/min in synthetic air before the adsorption of the reaction gas. The transient reaction of Methanol-SCR was monitored by FT-IR with gas composition as follows: NO + O_2 (500 ppm NO and 7% O_2 in N_2 atmosphere); $CH_3OH + O_2$ (1000 ppm CH_3OH and 7% O_2 in N_2 atmosphere), and N_2 balanced. Simultaneously, H_2O was introduced by bubbling with N_2 (1 mL/min) at 30 °C. The total flow rate of gas was 50 mL/min. The background spectrum was collected after the bubbling of H_2O with N_2 for 30 min before the reaction gas was flowed into the cell to perform in situ measurements. The perturbed T-O-T vibrational modes (1000 - 800 cm^{-1} in the IR spectra) of the zeolite framework to distinguish different Fe sites were obtained at 175 °C, and the background spectrum was collected without the sample in the synthetic air. The reducing and oxidizing half reactions of NO oxidation were monitored by FT-IR at 300 °C with gas composition in the following order: 14% O_2/N_2; 1000 ppm NO/N_2; 14% O_2/N_2). Prior to NH_3 adsorption experiments, the samples were evacuated (10^{-7} mbar) at 450 °C for 1 h. Then, FTIR spectra were acquired at 150 °C after adsorption of excess NH_3 (10 mbar). Extinction coefficient of 0.11 cm^2 $μmol^{-1}$ for NH_4^+ deforming vibration bands (1460 cm^{-1}) and 0.026 cm^2 $μmol^{-1}$ for NH_3 deforming vibration bands (1620 cm^{-1}) in IR spectra as described in previous publications, were employed to calculate the amount of Brønsted acid sites and Lewis acid sites, respectively[34].

Activity tests

Methanol-SCR reaction was executed in a fixed-bed reactor with the reactant gas mixture containing 2000 ppm CH_3OH, 1000 ppm NO, 14% O_2, and 5% H_2O in N_2 balance. 1000 ppm NO and 14% O_2 were used for the reaction of NO oxidation. The total flow rate of gas

through the catalysts was 1000 mL/min with a gas hourly space velocity (GHSV) of 30,000 h^{-1}. CH_3OH/H_2O solution was injected by a liquid plunger pump and flew through the evaporator. 2 mL of catalyst used for the catalytic activity test was prepared by pressing the catalyst powders under a pressure of 0.9 MPa, then pelletized and sieved to 18 ~ 30 mesh. The temperature was measured in the range of 200 °C to 500 °C. CH_3OH, CH_3OCH_3, CO, CO_2, NO, NO_2, and N_2O of the outlet gas were quantified by an FTIR spectrometer (Nicolet iS 10). HCHO of outlet gas was analyzed by a KITAGAWA gas detector tube (Komyo Rikagaku Kogyo). SO_2 poisoning of the Fe-FER catalyst was carried out under the conditions referred to in the previous work[39].

The bench test was conducted at the Shanghai Marine Diesel Engine Research Institute using a 150 × 150 × 150 mm monolithic catalyst coated with 0.6Fe-FER zeolite. The reaction condition refers to methanol engine exhaust parameters containing 2000 ppm CH_3OH, 1000 ppm NO, 14% O_2, 10% CO_2, and 5% H_2O in N_2 balance with a GHSV of 15, 000 h^{-1}.

The conversion of NO_x and N_2 yield were calculated by following equation:

$$NO_x\text{conversion}[\%] = \frac{NO_{x\ \text{inlet}} - NO_{x\ \text{outlet}}}{NO_{x\ \text{inlet}}} \times 100[\%] \quad (1)$$

$$N_2\text{yield}[\%] = \frac{NO_{x\ \text{inlet}} - NO_{x\ \text{outlet}} - 2 \times N_2O_{\text{outlet}}}{NO_{x\ \text{inlet}}} \times 100[\%] \quad (2)$$

The reaction rate was calculated using the following equation:

$$\text{Reactionrate}(\text{mmol} \cdot g^{-1} \cdot h^{-1}) = \frac{\text{Feed}_{NOx}\left(mL \cdot h^{-1}\right) \times X_{NOx}(\%)}{m_{catal}(g) \times 22.4(L \cdot mol^{-1}) \times 10^{-3}(mol \cdot mmol^{-1}) \times 10^{3}(mL \cdot L^{-1})} \quad (3)$$

where Feed_{NOx} represents the concentration of $NO_{x\ \text{inlet}}$, X_{NOx} represents the conversion of NO_x, m_{catal} represents the mass of catalyst.

Kinetic measurements

The limitations of internal and external diffusion were evaluated by reactions under different gas velocity and grain mesh before the kinetic measurements of the NO oxidation reaction. As shown in Fig. S37a, the conversions of NO are almost unchanged with different particle size from 40-100 mesh under GHSV = 30,000 h^{-1}. Thus, internal diffusion limitation was excluded with the particle size of 40-60 mesh. Furthermore, as shown in Fig. S37b, the conversions of NO are almost unchanged with the GHSV ≥ 800,000 h^{-1} indicating that the external diffusion limitation was also excluded with the GHSV = 800,000 h^{-1}. According to the above experiments, the GHSV and particle size were selected as 800, 000 h^{-1} and 40-60 mesh, respectively. Total gas flow through the catalysts was 1000 mL/min. The Arrhenius plots was drawn according to the reaction rate with the conversion of NO less than 20 %. The reaction order with respect to NO was also determined under the condition at 175 °C, a feed containing 14% O_2 with N_2 as balance gas was used and NO concentrations were varied in the range of 100-900 ppm.

Computation details

The FER zeolite model used for the adsorption of reaction gas was constructed by truncating a 60T cluster from the crystal structure. In order to reduce the computational cost, the computational model employed for the calculation of the reaction path was constructed by truncating an 18T cluster from the 60T cluster. One silicon atoms in the framework were replaced by one aluminum atom to construct H-FER zeolite model. Fe-FER zeolite was modeled by the construction of $[FeO]^+$ and Fe^{3+} sites at the G-site and B-site, respectively. Atoms far away from the reactants were kept fixed to their equilibrium positions during the optimization process for the skeleton stabilization. All of the associated structures were optimized at the level of DFT with Becke's three-parameter exchange and Lee-Yang-Parr correlation functional (B3LYP) implemented in the Gaussian 09 package[52]. The pseudo-potential basis set SDD was utilized for Fe, and the polarized 6-31 g (d, p) basis set was used for Si, Al, O, H, C, and N atoms. The combination of B3LYP/6-31 g (d, p) has been previously reported to provide accurate results in zeolite-catalyzed reactions[53,54]. Berny algorithms were adopted to search and optimize the transition states. The Hessian matrix was calculated to validate that only one imaginary frequency was observed for each transition state[55].

Data availability

The authors declare that the data supporting the findings of this study are available within the main article and the Supplementary Information. Data are available from the corresponding authors upon request. Source data are provided with this paper.

References

1. Bazaluk, O. et al. Assessment of green methanol production potential and related economic and environmental benefits: The case of China. *Energies* **13**, 3113 (2020).
2. Parris, D., Spinthiropoulos, K., Ragazou, K., Giovou, A. & Tsanaktsidis, C. Methanol, a plugin marine fuel for green house gas reduction—A review. *Energies* **17**, 605 (2024).
3. Krishna, S. H. et al. Influence of framework Al density in chabazite zeolites on copper ion mobility and reactivity during NO_x selective catalytic reduction with NH_3. *Nat. Catal.* **6**, 276–285 (2023).
4. Becher, J. et al. Chemical gradients in automotive Cu-SSZ-13 catalysts for NO_x removal revealed by operando X-ray spectro-tomography. *Nat. Catal.* **4**, 46–53 (2021).
5. Dann, E. K. et al. Structural selectivity of supported Pd nanoparticles for catalytic NH_3 oxidation resolved using combined operando spectroscopy. *Nat. Catal.* **2**, 157–163 (2019).
6. Ngo, A. B. et al. Effect of formaldehyde in selective catalytic reduction of NO_x by ammonia (NH_3-SCR) on a commercial V_2O_5-WO_3/TiO_2 catalyst under model conditions. *Environ. Sci. Technol.* **54**, 11753–11761 (2020).
7. Guo, K. et al. Conquering ammonium bisulfate poison over low-temperature NH_3-SCR catalysts: A critical review. *Appl. Catal. B-Environ.* **297**, 120388 (2021).
8. Männikkö, M., Wang, X., Skoglundh, M. & Härelind, H. Silver/alumina for methanol-assisted lean NO reduction—On the influence of silver species and hydrogen formation. *Appl. Catal. B-Environ.* **180**, 291–300 (2016).
9. Männikkö, M., Skoglundh, M. & Ingelsten, H. H. Selective catalytic reduction of NO_x with methanol over supported silver catalysts. *Appl. Catal. B-Environ.* **119**, 256–266 (2012).
10. Chansai, S. et al. Investigating the promotional effect of methanol on the low temperature SCR reaction on Ag/Al_2O_3. *Appl. Catal. B-Environ.* **160**, 356–364 (2014).
11. Han, F., Yuan, M. & Chen, H. Selective catalytic reduction of NO_x with methanol on H-ZSM-5: The effect of extra-framework aluminum. *Catal. Today* **355**, 443–449 (2020).
12. Wu, Y. et al. Interplay between copper redox and transfer and support acidity and topology in low temperature NH_3-SCR. *Nat. Commun.* **14**, 2633 (2023).
13. Han, L. et al. Selective catalytic reduction of NO_x with NH_3 by using novel catalysts: State of the art and future prospects. *Chem. Rev.* **119**, 10916–10976 (2019).
14. Catizzone, E. et al. Catalytic application of ferrierite nanocrystals in vapour-phase dehydration of methanol to dimethyl ether. *Appl. Catal. B- Environ.* **243**, 273–282 (2019).

15. Yarulina, I., Chowdhury, A. D., Meirer, F., Weckhuysen, B. M. & Gascon, J. Recent trends and fundamental insights in the methanol-to-hydrocarbons process. *Nat. Catal.* **1**, 398–411 (2018).
16. Fu, T., Shao, J. & Li, Z. Catalytic synergy between the low Si/Al ratio Zn/ZSM-5 and high Si/Al ratio HZSM-5 for high-performance methanol conversion to aromatics. *Appl. Catal. B-Environ.* **291**, 120098 (2021).
17. Li, S. et al. Brønsted/Lewis acid synergy in dealuminated HY zeolite: A combined solid-state NMR and theoretical calculation study. *J. Am. Chem. Soc.* **129**, 11161–11171 (2007).
18. Schallmoser, S. et al. Impact of the local environment of Brønsted acid sites in ZSM-5 on the catalytic activity in n-pentane cracking. *J. Catal.* **316**, 93–102 (2014).
19. Han, F. et al. Selective catalytic reduction of NO_x by methanol on metal-free zeolite with Brønsted and Lewis acid pair. *ACS Catal.* **12**, 2403–2414 (2022).
20. Sun, H. et al. Highly reactive methyl group drives selective catalytic reduction of NO_x by methanol on bismuth oxide nanoparticle implanted FER zeolite. *Appl. Catal. B-Environ.* **318**, 121883 (2022).
21. Hu, X. et al. Study on the catalytic activity and hydrothermal stability of one-pot synthesized Fe-based FER zeolites for NH_3-SCR. *Catal. Sci. Technol.* **13**, 5435 (2023).
22. Boubnov, A., Lichtenberg, H., Mangold, S. & Grunwaldt, J.-D. Identification of the iron oxidation state and coordination geometry in iron oxide- and zeolite based catalysts using pre-edge XAS analysis. *J. Synchrotron Rad.* **22**, 410–426 (2015).
23. Cheng, Q. et al. Maximizing active Fe species in ZSM-5 zeolite using organic template-free synthesis for efficient selective methane oxidation. *J. Am. Chem. Soc.* **145**, 5888–5898 (2023).
24. Dzwigaj, S., Stievano, L., Wagner, F. E. & Che, M. Effect of preparation and metal content on the introduction of Fe in BEA zeolite, studied by DR UV–vis, EPR and Mössbauer spectroscopy. *J. Phys. Chem. Solids* **68**, 1885–1891 (2007).
25. Zhang, J. et al. Synthesis, characterization and application of Fe-zeolite: A review. *Appl. Catal. A Gen.* **630**, 118467 (2022).
26. Tabor, E., Závěta, K., Sathu, N. K., Tvarůžková, Z. & Sobalík, Z. Characterization of iron cationic sites in ferrierite using Mössbauer spectroscopy. *Catal. Today* **169**, 16–23 (2011).
27. Ivanova, E. et al. Evidencing three distinct Fe II sites in Fe–FER zeolites by using CO and NO as complementary IR probes. *Appl. Catal. B-Environ.* **93**, 325–338 (2010).
28. Sazama, P. et al. Tailoring of the structure of Fe-cationic species in Fe-ZSM-5 by distribution of Al atoms in the framework for N_2O decomposition and NH_3-SCR-NO_x. *J. Catal.* **312**, 123–138 (2014).
29. Boroń, P. et al. BEA zeolite modified with iron as effective catalyst for N_2O decomposition and selective reduction of NO with ammonia. *Appl. Catal. B-Environ.* **138**, 434–445 (2013).
30. Dubkov, K. A., Ovanesyan, N. S., Shteinman, A. A., Starokon, E. V. & Panov, G. I. Evolution of iron states and formation of α-Sites upon Activation of FeZSM-5 Zeolites. *J. Catal.* **207**, 341–352 (2002).
31. Sobalík, Z., Tabor, E., Nováková, J., Sathu, N. K. & Závěta, K. Role of active oxygen and NO_x species in N_2O decomposition over Fe-ferrierite. *J. Catal.* **289**, 164–170 (2012).
32. Tabor, E. et al. Dioxygen dissociation over man-made system at room temperature to form the active-oxygen for methane oxidation. *Sci. Adv.* **6**, eaaz9776 (2020).
33. Zecevic, J., Vanbutsele, G., de Jong, K. P. & Martens, J. A. Nanoscale intimacy in bifunctional catalysts for selective conversion of hydrocarbons. *Nature* **528**, 245–248 (2015).
34. Zhao, G., Benhelal, E., Adesina, A., Kennedy, E. & Stockenhuber, M. Comparison of Direct, Selective Oxidation of Methane by N_2O over Fe-ZSM-5, Fe-Beta, and Fe-FER Catalysts. *J. Phys. Chem. C.* **123**, 27436–27447 (2019).
35. Shi, Z. et al. Generating silicon-rich AFX zeolite using rigid diquaternary alkylammonium structure directing agent towards stable selective catalytic reduction of NO_x by NH_3. *Appl. Catal. B-Environ.* **344**, 123637 (2024).
36. Janssens, T. V. W. et al. A consistent reaction scheme for the selective catalytic reduction of nitrogen oxides with ammonia. *ACS Catal.* **5**, 2832–2845 (2015).
37. Hu, H. et al. Mechanistic aspects of deNO_x processing over TiO_2 supported Co–Mn oxide catalysts: Structure–activity relationships and in situ DRIFTs analysis. *ACS Catal.* **5**, 6069–6077 (2015).
38. Wang, X., Jin, B., He, X., White, T. A. & Liang, X. Highly active and stable Fe/SiO_2 catalyst synthesized by atomic layer deposition for CO oxidation. *Catal. Lett.* **150**, 3296–3303 (2020).
39. Xu, L. et al. New insight into SO_2 poisoning and regeneration of CeO_2–WO_3/TiO_2 and V_2O_5–WO_3/TiO_2 catalysts for low-temperature NH_3–SCR. *Environ. Sci. Technol.* **52**, 7064–7071 (2018).
40. Hammershøi, P. S., Jangjou, Y., Epling, W. S., Jensen, A. D. & Janssens, T. V. W. Reversible and irreversible deactivation of Cu-CHA NH_3-SCR catalysts by SO_2 and SO_3. *Appl. Catal. B-Environ.* **226**, 38–45 (2018).
41. Wang, C. et al. Extra-framework aluminum-assisted initial C–C bond formation in methanol-to-olefins conversion on zeolite H-ZSM-5. *Angew. Chem.* **130**, 10354–10358 (2018).
42. Iwasaki, M. & Shinjoh, H. NO evolution reaction with NO_2 adsorption over Fe/ZSM-5: In situ FT-IR observation and relationships with Fe sites. *J. Catal.* **273**, 29–38 (2010).
43. Long, R. Q. & Yang, R. T. Selective catalytic reduction of NO with ammonia over Fe^{3+}-exchanged mordenite (Fe–MOR): Catalytic performance, characterization, and mechanistic study. *J. Catal.* **207**, 274–285 (2002).
44. Yasumura, S., Liu, C., Toyao, T., Maeno, Z. & Shimizu, K. -i Lean NO_x capture and reduction by NH_3 via NO^+ intermediates over H-CHA at room temperature. *J. Phys. Chem. C.* **125**, 1913–1922 (2021).
45. Zhang, Y. et al. Promotion of protolytic pentane conversion on H-MFI zeolite by proximity of extra-framework aluminum oxide and Brønsted acid sites. *J. Catal.* **370**, 424–433 (2019).
46. Wojtaszek, A., Sobczak, I. & Ziolek, M. NO adsorption combined with FTIR spectroscopy as a useful tool for characterization of niobium species in crystalline and amorphous molecular sieves. *Catal. Today* **192**, 149–153 (2012).
47. Xing, N., Wang, X., Zhang, A., Liu, Z. & Guo, X. Eley-Rideal mode of formamide species formation in selective catalytic reduction of NO by C_2H_2 over ferrierite based catalysts. *Catal. Commun.* **9**, 2117–2120 (2008).
48. Chen, H. et al. Effect of Ammonia on the Intermediates and Chemical Pathway of Selective Catalytic Reduction of NO by Ethanol over a Pt/Al_2O_3 Catalyst. *Energy Fuels* **36**, 9230–9242 (2022).
49. Li, J. et al. Investigation on deactivation periods of ZSM-5/SAPO-34 catalyst in MTA reaction: Carbon deposition behavior. *Fuel* **395**, 135207 (2025).
50. Ravel, B. & Newville, M. ATHENA, ARTEMIS, HEPHAESTUS: data analysis for X-ray absorption spectroscopy using IFEFFIT. *J. Synchrotron Radiat.* **12**, 537–541 (2005).
51. Klencsá, Z. et al. Interplay between magnetic order and the vibrational state of Fe in $FeCr_2S_4$. *J. Phys. Chem. Solids* **64**, 325–331 (2003).
52. Frisch. M. J. et al. Gaussian, Inc., Wallingford, CT 537-541 (2016).
53. Bao, X., Sung, C.-Y., Snurr, R. Q. & Broadbelt, L. J. Rate-determining step in the NO_x reduction mechanism on BaY zeolites and the importance of long-range lattice effects. *ACS Catal.* **2**, 350–359 (2012).
54. Fellah, M. F. Adsorption of hydrogen sulfide as initial step of H_2S removal: A DFT study on metal exchanged ZSM-12 clusters. *Fuel Process. Technol.* **144**, 191–196 (2016).
55. Schlegel, H. B. Optimization of equilibrium geometries and transition structures. *J. Comput. Chem.* **3**, 214–218 (2004).

Acknowledgements
This work was supported by the National Natural Science Foundation of China (Nos 22406092 to H.S., 22076081 to H.C. and 22272083 to W.D.), National Key Research and Development Program of China (2024YFE0206700 to H.S.), and China Postdoctoral Science Foundation (No. 2022M721704 to H.S.).

Author contributions
H.S. and D.L. designed the materials and carried out the experiments. C.L. performed materials synthesis. C.W. contributed to the collection and organization of all raw data in the present study. H.C., W.D., and G.H. supervised this project. Z.W. carried out the NMR experiments and analysis. M.K. provided help with XAFS tests. Y.H., X.L., K.L., H.Y., Z.X., and M.W. participated in the discussion and interpretation of experimental and theoretical data. H.S., D.L., H.C., G.H., and W.D. wrote the manuscript. All authors discussed the results and assisted with manuscript preparation.

Competing interests
The authors declare no competing interests.

Additional information
Supplementary information The online version contains supplementary material available at https://doi.org/10.1038/s41467-025-67458-1.

Correspondence and requests for materials should be addressed to Haijun Chen, Guangjin Hou or Weili Dai.

Peer review information *Nature Communications* thanks the anonymous reviewers for their contribution to the peer review of this work. A peer review file is available.